

Estimation of energy and moisture fluxes for dynamic vegetation using coupled SVAT and crop-growth models

Joaquin J. Casanova¹ and Jasmeet Judge¹

Received 7 September 2007; revised 17 November 2007; accepted 14 February 2008; published 26 July 2008.

[1] A Soil Vegetation Atmosphere Transfer (SVAT) model, viz. Land Surface Process (LSP) model, is coupled with a widely used crop-growth model, DSSAT, to estimate energy and moisture fluxes at the land surface and in the vadose zone for growing vegetation. In this study, we present detailed observations of soil and crop characteristics, and various components of energy and water balance during a season-long field experiment for sweet corn. The data set is used to calibrate the LSP with Latin Hypercube Sampling and Pareto ranking. We compare the observations with model estimates of crop growth and development, land surface fluxes, soil moisture and temperature profiles from both the stand-alone LSP and coupled LSP-DSSAT models. We find that the model estimates of radiation fluxes, soil moisture, and soil temperature, by both the LSP and LSP-DSSAT are very similar, indicating that the LSP-DSSAT model can be used to simulate fluxes for dynamic vegetation without the need of in situ vegetation observations. Moreover, because coupling was achieved without structurally changing either of the models, the methodology in this study can be extended to coupling other SVAT and vegetation growth models.

Citation: Casanova, J. J., and J. Judge (2008), Estimation of energy and moisture fluxes for dynamic vegetation using coupled SVAT and crop-growth models, *Water Resour. Res.*, 44, W07415, doi:10.1029/2007WR006503.

1. Introduction

[2] Soil Vegetation Atmosphere Transfer (SVAT) models simulate energy and moisture transport in soil and vegetation and estimate the fluxes at the land surface and in the vadose zone. The interactions between vegetation and the fluxes become increasingly important as these fluxes affect plant growth and development. Vegetation canopies impact latent and sensible heat fluxes, precipitation interception, and radiative transfer at the land-atmosphere interface, affecting soil moisture and temperature profiles in the vadose zone. These changing interactions during the growing season need to be included in the SVAT models, in order to provide realistic estimates of the fluxes.

[3] Different methodologies are used within SVAT models to simulate the effects of growing vegetation on land surface fluxes. Most SVAT models rely on observations or empirical functions to obtain vegetation conditions. For instance, in the Common Land Model (CLM) [Dai *et al.*, 2003], vegetated grid spaces are defined by patches of “plant functional types,” with parameters for physiological and structural properties associated with each type. The CLM allows for dynamic vegetation modeling for seasonal simulations through inputs of canopy properties and can be provided by vegetation models. This is an effective way to

perform global modeling of the land vegetative surface, and is capable of modeling long term biogeochemical interactions. However, because of the large time and space scales of the CLM, most of the vegetation parameters are empirical to meet computational constraints. A model developed by the National Centers for Environmental Prediction at Oregon State University, Air Force, and Hydrologic Research Laboratory at the National Weather Service (NOAH) simulates soil moisture and temperature profiles with a subdaily timestep, and with vegetation properties such as LAI, stomatal resistance, and roughness length defined by vegetation type classes [Pan and Mahrt, 1987].

[4] Coupling an SVAT model with a vegetation growth model allows inclusion of canopy effects without relying on observations or empirical functions. For example, Garcia-Quijano and Barros [2005] used a subdaily biochemical vegetation model with a land surface hydrology model. They modeled canopy transpiration and its influence on soil moisture and carbon fluxes. Mo *et al.* [2005] linked daily process-based crop models for summer maize and winter wheat with an hourly land surface flux model and a three-layer soil moisture model. In situ vegetation observations can still be used in such coupled models for validation.

[5] This study has two main objectives. First, an SVAT model is coupled with a crop growth simulation model to estimate land surface fluxes in growing vegetation and evaluate the performance of the coupled model for estimating root-zone soil moisture and ET observations from an extensive field experiment. Both categories of models benefit from two decades of development and testing by their respective research communities. The SVAT model, viz. Land Surface Process (LSP) model, simulates one-dimensional energy and moisture transport as well as

¹Center for Remote Sensing, Agricultural and Biological Engineering Department, Institute of Food and Agricultural Sciences, University of Florida, Gainesville, Florida, USA.

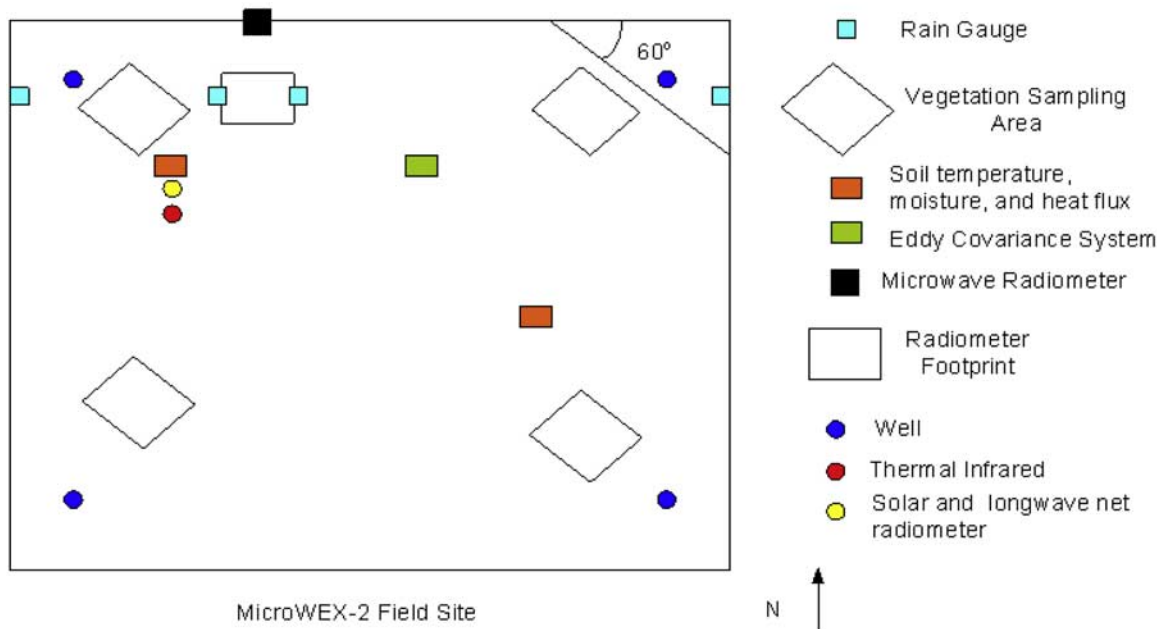


Figure 1. Instrumentation layout during MicroWEX-2.

radiative, sensible and latent heat fluxes at the land surface. The cropping system model, viz. the Decision Support System for Agrotechnology Transfer (DSSAT), is a widely used and tested modular suite of crop models that simulate crop growth (biomass accumulation) and development (vegetative and reproductive growth stages).

[6] Neither model is structurally changed and an interface is created to link the two models. In the coupled LSP-DSSAT model, the DSSAT model provides the LSP model with vegetation characteristics that influence heat, moisture, and radiation transfer at the land surface and in the vadose zone and the LSP model provides the DSSAT model with estimates of soil moisture and temperature profiles and evapotranspiration (ET). Here, we describe the coupling of the LSP and DSSAT models for different growth stages during a sweet corn (*Zea mays* var. *Rugosa*) growing season in North Central Florida. This study demonstrates that the LSP and DSSAT models can be coupled without compromising the flux estimates from the LSP model, and allow estimation of realistic water and energy transport without requiring in situ vegetation observations. Because neither model was structurally changed and an interface was created to allow the coupling and feedback between the two models, this methodology can be extended to coupling other SVAT and crop growth models.

[7] The second objective is the presentation of concurrent observations of various energy and water fluxes and vegetation parameters at high temporal resolution during a growing season of corn. Only a few similar data sets exist that provide such detailed measurements and allow future modeling studies involving other hydrology and corn growth models. In this study, we used the field observations to compare observed radiation and surface heat fluxes as well as soil moisture and temperature profiles during an extensive field experiment to those estimated by both the

coupled LSP-DSSAT model and by the stand-alone LSP model that was forced with observed vegetation parameters.

2. Second Microwave Water and Energy Balance Experiment

[8] MicroWEX-2 was conducted from Day of Year (DoY) 78 (18 March) to DoY 154 (June 2) in 2004 by the Center for Remote Sensing to monitor micrometeorological, soil, and vegetation conditions as well as the microwave brightness temperatures during a growing season for sweet corn of variety Saturn SH2 [Judge *et al.*, 2005]. The experimental site (Figure 1) was a 3.6 hectare (9 acre) field located at the UF/IFAS Plant Science Education and Research Unit (PSREU), in North Central Florida (29.41°N, 82.18°W). The soils at the site are lake fine sand with about 90% sand and a bulk density of 1.55 g/cm³. Row spacing was 76 cm, with approximately eight plants per square meter. Irrigation and fertigation were conducted via a linear move system. Data collected during MicroWEX-2 included soil moisture, temperature and heat flux, latent and sensible heat flux, wind speed and direction, upwelling and downwelling short and longwave radiation, precipitation, irrigation, water table depth, and microwave brightness at 6.7 GHz ($\lambda = 4.47$ cm), every 15 min. The soil moisture, heat fluxes, and temperatures were observed at two locations in the field. Soil moisture and soil temperature were observed at 2, 4, 8, 16, 32, 64, and 100 cm using Campbell Scientific Water Content Reflectometers and Vitel Hydra-probes; and thermistors and thermocouples, respectively. An Eddy covariance system measured wind speed, direction, and latent and sensible heat fluxes. REBS CNR net radiometer measured up- and down- welling short- and long- wave radiation. Everest Interscience infrared sensor measured thermal infrared temperature. Four tipping-bucket rain gauges logged precipitation at four locations East and West of the

Table 1. Measurement Uncertainties During MicroWEX-2

Sensor	Uncertainty	Reference
Raingauge	12 mm/h	<i>Nyusten et al.</i> [1996]
TDR	0.025 VSM	<i>Campbell Scientific</i> [2006]
Thermistor	0.1 K	<i>Omega</i> [2006]
Soil heat flux	15 W/m ²	<i>Twine et al.</i> [2000]
Net radiation	22 W/m ²	<i>Twine et al.</i> [2000]
Latent heat flux	11.1–28.0 W/m ²	<i>Richardson et al.</i> [2006]
Sensible heat flux	14.5–22.7 W/m ²	<i>Richardson et al.</i> [2006]

footprint, and at the East and West sides of the field. Water table depth was measured using Solinst Level Loggers in a monitoring well in each quadrant. The University of Florida's C-band microwave radiometer measured vertically and horizontally polarized microwave emissions from an area of 8.54 m by 8.54 m in the northwest area of the corn field from a height of 6.17 m.

[9] In addition to continuously logged data, there were also weekly vegetation and twice-weekly soil samplings. Vegetation sampling was conducted in four areas, one in each quadrant of the field. Samples were selected by placing a meter stick halfway between two plants and ending the sample at least 1 m from the starting point and halfway between two plants. The actual row length of the sample was noted. We measured stand density, leaf number, canopy height and width, wet and dry weights of leaves, stems, and ears. Two LAI measurements were taken in each sampling area using the Licor LAI-2000 Canopy Analyzer. Root length density was measured in the vadose zone at tasseling. Nitrogen was measured in each of the four wells before and

after MicroWEX-2. Table 1 shows the uncertainties in the measurements for the sensor data used in this study.

3. LSP Model

[10] The LSP model was originally developed by the Microwave Geophysics Group at the University of Michigan [Liou et al., 1998]. The model simulates 1-d coupled energy and moisture transport in soil and vegetation, and estimates energy and moisture fluxes at the land surface and in the vadose zone. It is forced with micrometeorological parameters such as air temperature, relative humidity, downwelling solar and longwave radiation, irrigation/precipitation, and windspeed. The original version has been rigorously tested [Judge et al., 2003] and extended to wheat-stubble [Judge et al., 1999] and brome-grass [Judge et al., 2008] in the Great Plains, prairie wetlands in Florida [Whitfield et al., 2006], and to tundra in the Arctic [Chung, 2007].

[11] In this study, a new version of the LSP model was used with a modified radiation flux parameterization at the land surface. Specifically, the shortwave radiative transfer was altered to a more physically based formulation, including both diffuse and direct radiation, and canopy transmissivity described by *Campbell and Norman* [1998]. The original version of the LSP model followed a more empirically based formulation by *Verseghy et al.* [1993]. In addition, the aerodynamic resistances and the surface vapor resistances were changed in the new version to extend it to tall vegetation and to partially vegetated terrain [Goudriaan, 1977]. The original version was developed for homogeneous land cover, such as bare soil or short grass. The new version of the model also includes adaptive timesteps for computational efficiency and to allow sudden changes or

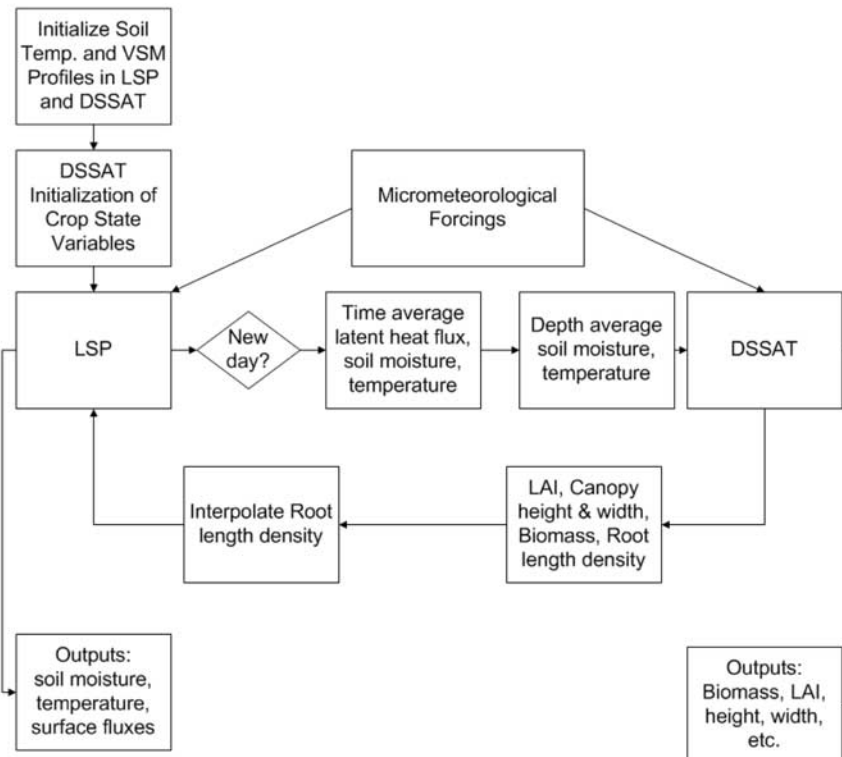
**Figure 2.** Algorithm for the coupling of the LSP and DSSAT models.

Table 2. Values for Soil Properties (Constrained) in the LSP Model

Parameter	Description	0–1.7 m	1.7–2.7 m
λ	poresize index	0.27	0.05
ψ_0	air entry pressure (m H ₂ O)	0.076	0.019
K_{sat}	saturated hydraulic conductivity (m/s)	2.06×10^{-4}	8.93×10^{-5}
θ_r	volumetric wilting point moisture (m ³ /m ³)	0.0051	0.0040
θ_{sat}	volumetric saturation moisture (m ³ /m ³)	0.34	0.41
ϕ_{sa}	volumetric sand fraction (m ³ /m ³)	0.894	0.512
ϕ_{si}	volumetric silt fraction (m ³ /m ³)	0.034	0.083
ϕ_c	volumetric clay fraction (m ³ /m ³)	0.071	0.405
ϕ_o	volumetric organic fraction (m ³ /m ³)	0.000	0.000
ϕ	porosity	0.34	0.41

large fluxes in our sandy soils with high thermal and hydraulic conductivities. The following section provides a description of the modified LSP model used in this study. Fundamental governing equations are also included in the section for completeness even though they remain unchanged from the original version.

3.1. Energy and Moisture Transport at the Land Surface

3.1.1. Energy Balance

[12] Combining the radiation and heat flux boundary conditions, the net energy flux into the canopy ($Q_{net,c}$) and soil ($Q_{net,s}$) (W/m²):

$$Q_{net,c} = H_{sc} + R_{s,c} + R_{l,c} - H_{ca} - LE_{tr} - LE_{ev} \quad (1)$$

$$Q_{net,s} = -H_{sc} + R_{s,s} + R_{l,s} - H_{sa} - LE_s \quad (2)$$

where H_{sc} , H_{ca} , and H_{sa} are the sensible heat fluxes between soil and canopy, canopy and air, and soil and air, respectively; LE_{tr} , LE_{ev} , and LE_s are the latent heat fluxes from transpiration, canopy evaporation, and soil evaporation, respectively; and $R_{s,c}$, $R_{s,s}$, $R_{l,c}$, $R_{l,s}$ are the net solar radiation intercepted by the canopy, intercepted solar radiation by the soil, net longwave radiation at the canopy, and net longwave at the soil, respectively. The details of the calculation of the energy fluxes are included in Appendices A–D.

3.1.2. Moisture Balance

[13] The net infiltration of moisture at the soil surface ($I_{net,s}$) is given by:

$$I_{net,s} = Pf_B + D - R - E_s \quad (3)$$

where P is the precipitation, D is the canopy drainage from the canopy to the soil, R is the runoff, and E_s is the soil evaporation. D given by $W_r - W_{r,max}$. The rate of change in moisture intercepted by the canopy is given by

$$\frac{dW_r}{dt} = Pf_v - D - E_{ev} \quad (4)$$

3.2. Soil Processes

[14] Heat and moisture transport in the soil is determined as the numerical solution to [Philip and de Vries, 1957]:

$$\frac{\partial \theta}{\partial t} = -\nabla q_m \quad (5)$$

$$C_{v,s} \frac{\partial T}{\partial t} = -\nabla q_h \quad (6)$$

$$q_m = q_l + q_v \quad (7)$$

$$q_l = -D_{\theta,l} \nabla \theta - D_{T,l} \nabla T + K + S \quad (8)$$

$$q_v = -D_{\theta,v} \nabla \theta - D_{T,v} \nabla T \quad (9)$$

$$q_h = -\kappa \nabla T + \rho \lambda q_v + C_{v,w} (T - T_0) q_m \quad (10)$$

where q_l , q_v , and q_h are liquid, vapor, and heat fluxes, respectively; T and θ are temperature and volumetric soil moisture, respectively. $D_{\theta,l}$ is the diffusivity of liquid under

Table 3. Sampling Ranges From [Goudriaan, 1977] and Values for Calibrated Parameters in the LSP Model

Parameter	Description	Sampling Range	Calibrated Value
z_{ob}	bare soil roughness length, m	$10^{-4} - 10^{-2}$	0.004
x	leaf angle distribution parameter	$10^{-2} - 2.0$	0.819
σ	leaf reflectance	$10^{-2} - 0.5$	0.474
ϵ_c	canopy emissivity	0.95–0.995	0.973
ϵ_s	soil emissivity	0.95–0.995	0.953
c_d	canopy drag coefficient	$10^{-5} - 1.0$	0.328
i_w	canopy wind intensity factor	$10^{-3} - 10^2$	67.90
l_w	leaf width, m	$10^{-3} - 10^{-1}$	0.0531
F_b	base assimilation rate, kg CO ₂ /m ² s	$-10^{-8} - 10^{-10}$	-8.20×10^{-9}
ϵ_{photo}	photosynthetic efficiency (kg CO ₂ /J)	$10^{-7} - 10^{-5}$	8.97×10^{-7}
$soil_a$	slope parameter for r_s , m ² s/kg H ₂ O	$0.0 - 5 \times 10^3$	3700.0
$soil_b$	intercept parameter for r_s , m ² s/kg H ₂ O	$0.0 - 6 \times 10^2$	-531.0

Table 4. Cultivar Coefficient Values in the Calibrated CERES-Maize Model

Cultivar Coefficient	Value
P1	157.20
P2	1.000
P5	811.20
G1	853.00
G3	10.4
PHINT	40.33

a moisture gradient; $D_{T,l}$ is the diffusivity of liquid under a temperature gradient; $D_{\theta,v}$ is the diffusivity of vapor under a moisture gradient; $D_{T,v}$ is the diffusivity of vapor under a temperature gradient, from [Philip and de Vries, 1957]; K is hydraulic conductivity, from [Rossi and Nimmo, 1994]; κ is thermal conductivity of soil from [de Vries, 1963], S is a sink term (root water uptake), and $C_{v,s}$ is the volumetric heat capacity of soil. $C_{v,w}$, ρ , and λ are the heat capacity, density, and heat of vaporization of water.

[15] The soil profile is defined with layers of different constitutive properties, divided into computational blocks, with the thickness of blocks increasing exponentially with depth. The coupled heat and moisture transport equations are solved using a block-centered, forward-time finite difference scheme. The upper boundary condition is a heat and moisture flux determined by the meteorological forc-

ings, while the lower boundary condition (2.7 m for this study) assumes free flow of heat and moisture.

4. DSSAT Model

[16] DSSAT is a modular crop simulation model with modules for soil, soil-plant-atmosphere, weather, management, and crop development and growth. The soil module simulates soil moisture using a bucket model and soil temperature as an empirical function of air temperature and depth. The soil-plant-atmosphere module estimates ET. In the weather module, meteorological forcings are read in, and in the management module, irrigation, fertilization, and pest control are read or generated. The crop module simulates the phenological development and growth, on a daily timestep, of a number of different crops, including soybeans, wheat, and cotton [Jones et al., 2003]. CERES-Maize [Jones and Kiniry, 1986] is a part of the crop growth submodule that simulates corn growth and development. CERES-Maize uses three files for determining growth and development characteristics: the species file, the ecotype file, and the cultivar file. The species file contains defining characteristics of corn, including root growth parameters, seed initial conditions, nitrogen and water stress response coefficients, nitrogen uptake parameters, base and optimum temperatures for grain fill and photosynthesis, and radiation and CO₂ parameters governing photosynthesis. The ecotype file specifies thermal time development, radiation use efficiency, and light extinction

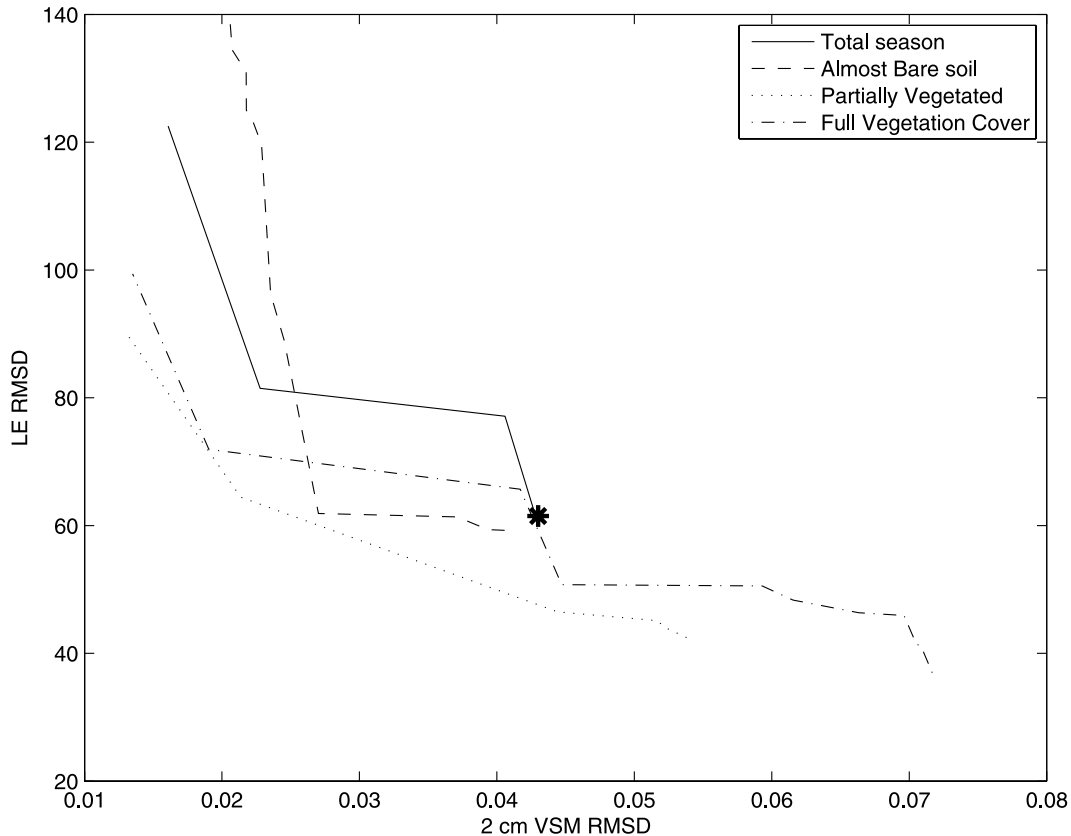


Figure 3. Pareto fronts from calibration of the stand-alone LSP model. The asterisk represents the point on the Pareto front where the total seasonal RMSD for 2 cm VSM is 0.043 m³/m³.

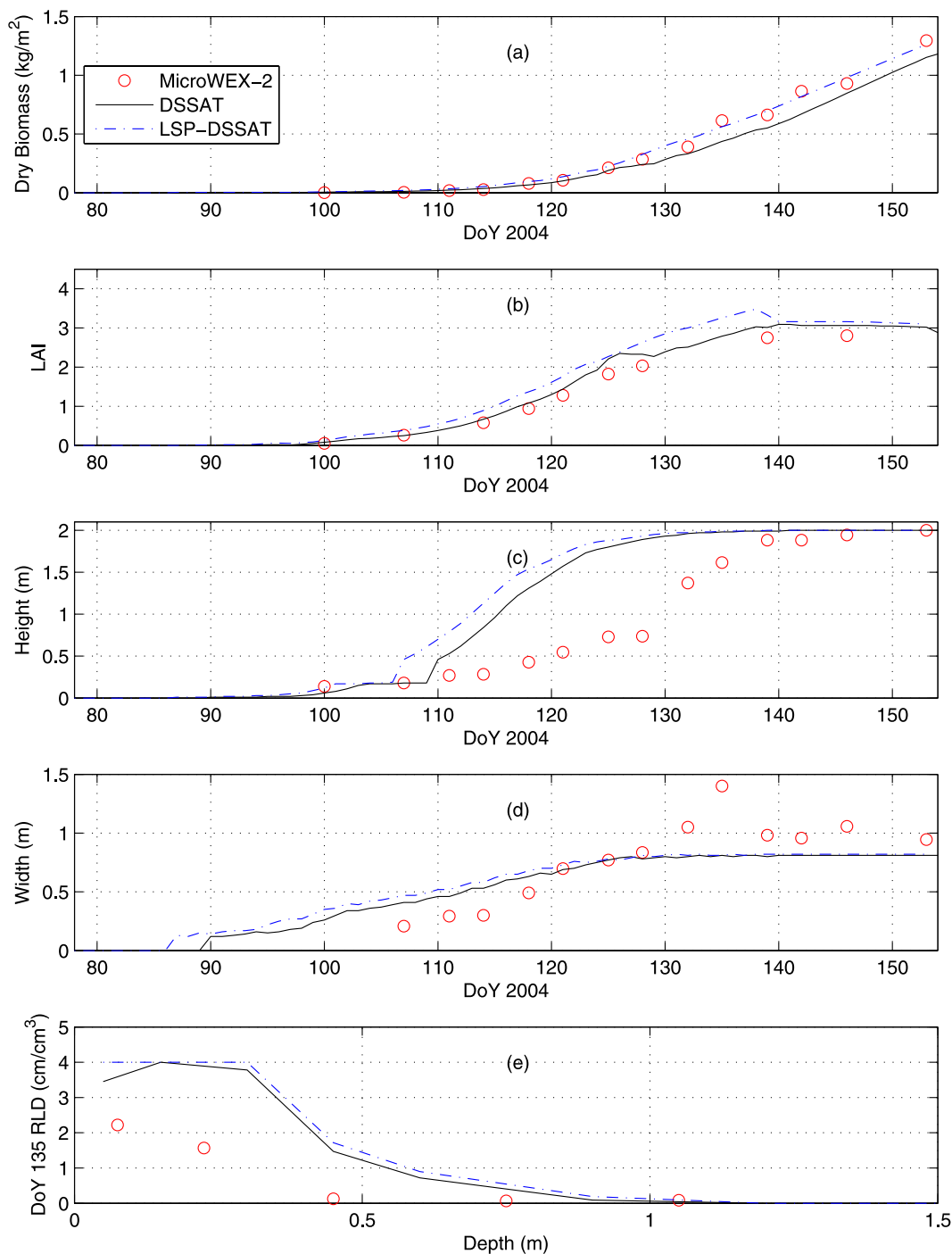


Figure 4. Comparison of estimations by the coupled LSP-DSSAT and stand-alone DSSAT model simulation and those observed during MicroWEX-2: (a) dry biomass, (b) LAI, (c) height, (d) width, and (e) the root length density (RLD) profile on DoY 135.

coefficients for three main types of corn. The cultivar file specifies the six cultivar coefficients that describe growth and development characteristics for different maize cultivars.

[17] P1: degree days between emergence and end of juvenile stage.

[18] P2: development delay for each hour increase in photoperiod past optimum photoperiod.

[19] P5: degree days from silking to maturity.

[20] G2: maximum possible number of kernels per plant.

[21] G3: kernel filling rate during the linear grain filling stage and under optimum conditions (mg/d).

[22] PHINT: phyllochron interval, i.e., the interval in thermal time (degree days) between leaf tip appearances.

[23] Corn growth and development is marked by eight events: germination, emergence, end of juvenile phase, floral induction (tassel initiation), 75% silking, beginning grain fill, maturity, and harvest. Transition from one devel-

Table 5. Comparison of dry Biomass, LAI, Height, Width, and Evapotranspiration (ET) From Stand-Alone DSSAT and the Coupled LSP-DSSAT Models With Observations During MicroWEX-2

	Stand-Alone DSSAT			Coupled LSP-DSSAT		
	RMSD	MAD	Bias	RMSD	MAD	Bias
Total biomass, kg/m ²	0.090	0.063	-0.059	0.052	0.040	0.005
LAI (-)	0.22	0.18	0.18	0.42	0.38	0.13
Height, m	0.61	0.45	0.44	0.70	0.54	0.54
Width, m	0.23	0.18	-0.06	0.24	0.19	-0.04
ET, mm	1.63	1.36	0.31	1.64	1.25	0.62

opmental stage to the next is determined by the growing degree days (GDD) with a base temperature of 8°C. Vegetative growth stops on 75% silking, when reproductive growth begins in the form of grain fill. Yield is the grain-fill value at harvest. Threshold GDD for each stage and grain fill parameters are contained in a cultivar file. The model determines total dry biomass using the radiation use efficiency method, in which half of the total solar radiation is taken as photosynthetically active radiation (PAR), and the fraction of PAR intercepted by the canopy is calculated from LAI using Beer's Law. Dry matter accumulation rate is a product of radiation use efficiency and a conversion factor. The CERES-Maize model determines LAI by tracking the total number of leaves, and calculating a leaf area growth rate, so that the rate of increase of LAI is the product of leaf area growth and current leaf number. Leaf growth is partly determined by the GDD between successive leaf tip appearances, called the phyllochron interval. In addition, a leaf senescence rate is calculated based on water stress. A canopy height and width model was added to the standard CERES model within DSSAT 4.0 following *Lizaso et al.* [2005].

5. Coupling of LSP and DSSAT Models

[24] Both the LSP and the DSSAT models are forced with micrometeorological conditions provided in each model's required format. A flowchart of the model coupling is shown in Figure 2. The soil moisture and temperature profiles are initialized in both models. The LSP model simulates energy and moisture fluxes using an adaptive timestep. At the last timestep of each day, the daily averages of ET, soil moisture and soil temperature are calculated and passed on to the DSSAT model. The DSSAT uses these values in calculating growth rates to obtain the crop variables such as biomass, LAI, etc. using a daily timestep. The estimates of biomass (used for canopy heat capacity), root-length densities (used for root water uptake), LAI (used

for radiation balance), height and width (used for aerodynamic resistance) are provided to the LSP model for flux estimation on the next day.

[25] The main challenge in coupling an SVAT model such as the LSP and a crop model such as the DSSAT arises from the difference in timestep and thickness of soil nodes between the two models. The LSP model uses short timesteps (on the order of seconds) and a user-defined number of nodes (35 in the top 1.8 m for this study). DSSAT uses daily timesteps, with 9 nodes in the top 1.8 m. In our coupling, the LSP model essentially replaces the soil and soil-plant-atmosphere modules of the DSSAT model. To account for the timestep difference, the soil moisture and temperature profiles estimated by the LSP model are averaged daily. The latent heat fluxes are accumulated daily and converted from W/m² to mm/day, treating soil and vegetation latent heat fluxes separately so that it can match the DSSAT requirements. To account for the difference in thickness of soil nodes, we spatially average the daily averages of soil moisture and temperature profiles from the LSP to match the soil nodes in the DSSAT. In addition, the root length density for the 9 DSSAT nodes are interpolated/extrapolated to match the LSP nodes. Because the LSP model does not include nitrogen transport in canopy and soil, the DSSAT model is run assuming there is no nitrogen stress. This is a reasonable assumption for heavily fertigated soils, such as ours during MicroWEX-2.

6. Methodology

[26] In this study, the model simulations were conducted using two scenarios. First, using a stand-alone LSP simulation forced with vegetation parameters observed during MicroWEX-2 and second, using the coupled LSP-DSSAT model.

6.1. Inputs and Initial Conditions

[27] Both the LSP and LSP-DSSAT models were run from planting on DoY 78, to harvest on DoY 154, 2004.

Table 6. Comparison of Surface Fluxes (W/m²) Estimated by the Coupled LSP-DSSAT Model With Those Observed During MicroWEX-2 at Different Stages of Growth

Flux	DoY 78–105			DoY 105–125			DoY 125–135			DoY 135–155		
	RMSD	MAD	Bias	RMSD	MAD	Bias	RMSD	MAD	Bias	RMSD	MAD	Bias
Net radiation	31.94	20.13	15.12	28.53	21.68	20.16	17.37	14.75	10.89	17.46	14.00	2.78
Latent heat flux	65.23	51.02	15.26	59.18	47.90	23.45	61.50	44.80	3.04
Sensible heat flux	47.36	37.98	29.20	57.10	44.04	34.88	75.61	60.37	59.33
Soil heat flux	48.35	25.45	-2.45	38.15	22.09	-6.25	43.90	26.51	0.42	54.01	26.94	2.20

Table 7. Comparison of Soil Moisture (m^3/m^3) Estimated by the Coupled LSP-DSSAT Model With Those Observed During MicroWEX-2 at Different Stages of Growth

Depth, cm	DoY 78–105			DoY 105–125			DoY 125–135			DoY 135–155		
	RMSD	MAD	Bias	RMSD	MAD	Bias	RMSD	MAD	Bias	RMSD	MAD	Bias
2	0.037	0.036	0.036	0.034	0.031	0.031	0.049	0.047	0.047	0.063	0.063	0.063
4	0.020	0.018	0.018	0.019	0.014	0.014	0.040	0.037	0.037	0.052	0.051	0.051
8	0.023	0.020	0.020	0.016	0.013	0.005	0.043	0.041	0.041	0.055	0.054	0.054
32	0.028	0.028	0.028	0.024	0.023	0.023	0.031	0.030	0.030	0.043	0.042	0.042
64	0.053	0.052	0.052	0.055	0.055	0.055	0.059	0.059	0.059	0.077	0.077	0.077
100	0.040	0.040	0.040	0.050	0.050	0.050	0.055	0.055	0.055	0.085	0.084	0.084

Micrometeorological forcings were obtained from observations during MicroWEX-2, and from a nearby weather station, installed as part of the Florida Automated Weather Network (FAWN). The precipitation/irrigation observations exhibited most variability between the four raingauges (Figure 1). To obtain forcings for the model simulations, we confirmed that rain gauge data coincided with the observed soil moisture increases. The data were scaled such that the daily accumulated observations from the raingauges matched those observed independently at the same field site using collection cans.

[28] Initial conditions were not known during MicroWEX-2 because our sensor installation was completed 7 d after planting. The first values observed by the soil moisture and temperature sensors were used as the initial moisture and temperature values for the simulations.

[29] Soil physical properties were based on texture and retention curve measurements taken from soil samples in the field at different depths, and are listed in Table 2.

6.2. Calibration

[30] The DSSAT and the LSP models were calibrated separately for the entire growing season. In the DSSAT model, six corn cultivar coefficients governing the growth and development, as described in section 4, were calibrated using Simulated Annealing to minimize the root mean square difference (RMSD) between modeled and observed LAI and biomass during MicroWEX-2. Detailed calibration methodology for the DSSAT model is described by Casanova *et al.* [2006].

[31] The stand-alone LSP model was calibrated, using observed vegetation parameters during MicroWEX-2, with repeated Latin Hypercube Sampling of the parameter space [McKay *et al.*, 2000]. Twelve parameters were calibrated in the model; four of these parameters were related to radiation

balance: leaf reflectance, σ , leaf angle distribution, x , soil emissivity, ϵ_s , and canopy emissivity, ϵ_c . The remaining eight parameters were related to sensible and latent heat fluxes: canopy base assimilation rate, F_b , photosynthetic efficiency, ϵ_{photo} , bare soil aerodynamic roughness, z_{ob} , leaf width, l_w , wind intensity factor, i_w , canopy drag coefficient, c_d , and soil evaporation resistance parameters, $soil_a$ and $soil_b$. The calibration of these parameters was conducted to minimize RMSDs between the modeled and observed volumetric soil moisture (VSM) at 2 cm and latent heat flux (LE) for the overall growing season. These two objectives were chosen because VSM is one of the most important factors governing the moisture and energy fluxes, and in our calibration we found VSM and LE to be competing objectives. The LE observations with low friction velocity ($u^* < 0.1$ m/s) were filtered.

[32] During the calibration, 5000 points were sampled in the form of twenty 250-point Latin Hypercube Samples within the ranges from Goudriaan [1977], specified in Table 3, using the University of Florida's High-Performance Computing Center. These sampled points were ordered by Pareto ranking and the set of points with the lowest Pareto rank were considered as the optimal parameter set [Gupta *et al.*, 1999].

7. Results and Discussion

7.1. Calibration

7.1.1. DSSAT

[33] Table 4 provides the calibrated values of the six cultivar coefficients in the DSSAT model, as obtained from Casanova *et al.* [2006]. These values were used in this paper for simulations using both stand-alone DSSAT and coupled LSP-DSSAT models.

7.1.2. LSP

Table 8. Comparison of Soil Temperature (K) Estimated by the Coupled LSP-DSSAT Model With Those Observed During MicroWEX-2 at Different Stages of Growth

Depth, cm	DoY 78–105			DoY 105–125			DoY 125–135			DoY 135–155		
	RMSD	MAD	Bias	RMSD	MAD	Bias	RMSD	MAD	Bias	RMSD	MAD	Bias
2	2.19	1.73	1.37	1.47	1.10	−0.06	2.38	1.87	1.48	3.38	3.03	2.92
4	2.49	1.87	1.34	1.60	1.29	−0.41	2.43	1.96	1.14	3.43	2.96	2.91
8	1.88	1.44	1.14	1.22	0.98	−0.37	2.00	1.59	1.15	3.41	3.13	3.13
32	1.19	1.01	0.97	0.91	0.75	−0.51	1.32	1.07	0.41	2.88	2.79	2.79
64	0.84	0.72	0.69	0.79	0.65	−0.54	0.92	0.79	−0.07	2.47	2.41	2.41
100	0.25	0.22	0.11	1.06	0.94	−0.94	0.84	0.79	−0.72	1.75	1.66	1.66

Table 9. Comparison of Surface Fluxes (W/m^2) Estimated by the Stand Alone LSP and Coupled LSP-DSSAT Model With Those Observed During MicroWEX-2

Flux	Stand-Alone LSP			Coupled LSP-DSSAT		
	RMSD	MAD	Bias	RMSD	MAD	Bias
Net radiation	23.86	16.11	10.38	25.62	18.12	12.65
Latent heat flux	58.55	45.40	12.15	62.45	48.93	16.59
Sensible heat flux	53.75	43.44	36.65	55.86	43.44	35.58
Soil heat flux	47.68	26.24	-1.54	46.54	25.02	-1.83

[34] The result of our multiobjective calibration was a Pareto front [Gupta *et al.*, 1999]. Figure 3 shows the Pareto fronts for the overall growing season with RMSDs between the model estimates and observations of the two objectives, VSM at 2 cm and LE. One set of calibrated parameters were obtained for the whole growing season, and we divided the growing season into four periods to understand the differences in Pareto fronts during different growth stages (Figure 3). These four stages include: almost bare soil (DoY 78–105), intermediate vegetation cover (DoY 105–125), full vegetation cover (DoY 125–135), and reproductive stage (DoY 135–154). A Pareto front could not be generated for the reproductive stage due to lack of LE observations during this stage. In general, the fronts show that the model performs best during the intermediate cover stage, with the front closest to the origin. The front for the bare soil stage is farthest from the origin for very low moisture RMSDs ($<0.026 \text{ m}^3/\text{m}^3$) and the front during the full vegetation cover is the farthest for higher moisture RMSDs ($>0.026 \text{ m}^3/\text{m}^3$).

[35] For the stand-alone LSP and LSP-DSSAT simulations in this study, we used the Pareto front for the overall season in Figure 3 and chose the 12 parameter values corresponding to an RMSD in VSM at 2 cm of $0.043 \text{ m}^3/\text{m}^3$, noted by an asterisk in the figure. This choice was based upon the sensitivity of SVAT models to VSM for hydrometeorological applications [Leese *et al.*, 2001; Kerr *et al.*, 2001; Entekhabi *et al.*, 2004]. With the RMSD in VSM of $0.043 \text{ m}^3/\text{m}^3$, we can expect an RMSD in latent heat flux of $\sim 60 \text{ W}/\text{m}^2$ for the overall season and about 60, 50, and $60 \text{ W}/\text{m}^2$ for the first three stages, respectively (see Figure 3). Table 3 lists the calibrated parameter values used in the LSP and LSP-DSSAT model simulations.

7.2. Model Simulation

7.2.1. DSSAT

[36] The DSSAT model provided realistic estimates of growth and development of sweet corn. The stand-alone

DSSAT estimated the emergence date on DoY 90 and LSP-DSSAT estimated the emergence date on DoY 87, compared to DoY 86 observed during MicroWEX-2. The coupled LSP-DSSAT model estimates higher soil temperatures in the top 30 cm that those estimated by the stand-alone DSSAT model in the top 30 cm (by about 3 K) resulting in an earlier emergence estimate. Modeled anthesis day, when 75% of the corn has silked, was DoY 139, while we observed 75% silking on DoY 135.

[37] Figures 4a–4e show the comparison of estimates of dry biomass, LAI, canopy height, canopy width, and root length density profiles on DoY 135, by the stand-alone DSSAT model, by the LSP-DSSAT model, and those observed during MicroWEX-2. Estimates from both model simulations compared well with the observations with RMSDs of <0.5 for LAI and $<0.10 \text{ kg}/\text{m}^2$ for dry biomass (see Table 5). The estimates from the two models differed by <0.2 for LAI and $<0.06 \text{ kg}/\text{m}^2$ for dry biomass, with the coupled LSP-DSSAT model estimating higher values than the stand-alone DSSAT. Similarly, the LSP-DSSAT model also estimates higher values of height, width, and root length density than the DSSAT model (see Table 5). These relatively small differences could be due to higher daily averages of soil moisture in the LSP-DSSAT than those in the stand-alone DSSAT's bucket model, by $>0.02 \text{ m}^3/\text{m}^3$. The higher soil moisture values would permit increased growth resulting in higher LAI and dry biomass in the coupled model. The high moisture estimates also result in higher daily ET in the coupled model compared to the DSSAT (Table 5). The LSP-DSSAT predicts $<0.5 \text{ mm}/\text{d}$ higher ET than DSSAT alone, with the RMSD between the daily estimates of ET by the LSP-DSSAT and observations of 1.69 mm.

7.2.2. LSP-DSSAT Model

[38] We evaluated the performance of the coupled LSP-DSSAT model by comparing its estimates of surface fluxes, soil moisture, and temperature profiles to those observed

Table 10. Comparison of Volumetric Soil Moisture (m^3/m^3) Estimated by the Stand Alone LSP and Coupled LSP-DSSAT Model With Those Observed During MicroWEX-2

Depth, cm	Stand-Alone LSP			Coupled LSP-DSSAT		
	RMSD	MAD	Bias	RMSD	MAD	Bias
2	0.047	0.044	0.044	0.046	0.043	0.043
4	0.035	0.029	0.029	0.034	0.028	0.028
8	0.036	0.030	0.028	0.036	0.030	0.028
32	0.032	0.031	0.031	0.032	0.031	0.030
64	0.062	0.061	0.061	0.062	0.061	0.061
100	0.060	0.057	0.057	0.060	0.057	0.057

Table 11. Comparison of Soil Temperature (K) Estimated by the Stand Alone LSP and Coupled LSP-DSSAT Model With Those Observed During MicroWEX-2

Depth, cm	Stand-Alone LSP			Coupled LSP-DSSAT		
	RMSD	MAD	Bias	RMSD	MAD	Bias
2	2.80	2.22	1.90	2.43	1.91	1.37
4	2.88	2.21	1.73	2.56	2.00	1.21
8	2.60	2.03	1.73	2.27	1.77	1.22
32	2.03	1.56	1.40	1.76	1.41	0.93
64	1.70	1.24	1.09	1.45	1.15	0.67
100	1.26	0.91	0.44	1.12	0.90	0.09

during MicroWEX-2, and to those estimated by the stand-alone simulation of the LSP model. In this section, we discuss these comparisons during the four growth stages and during the entire growing season separately to provide detailed insight into modeled fluxes during different growing stages. The model simulations were conducted using calibrated parameter values given in Table 3. This section discusses statistics for coupled LSP-DSSAT model simulation, but Tables 6–11 provide detailed statistics for both the coupled LSP-DSSAT and the stand-alone LSP model simulation.

7.2.2.1. Early Season: Almost Bare Soil

[39] This period included the first 27 d of the growing season (DoY 78–105), when it was “almost” bare soil with low vegetation. The canopy height was <17 cm, LAI was <0.2, and vegetation cover was <0.22. (Figures 5a and 5b) show the estimated and observed net radiation as well as residuals (LSP-DSSAT minus observed) during this period, respectively. Overall, both the coupled and the stand alone models capture the phases of the diurnal variation in net radiation. The RMSDs between the model estimates and observations are similar for both models’ simulations (coupled LSP-DSSAT and stand-alone LSP) at $\sim 32 \text{ W/m}^2$. However, the peak daytime differences are as high as 100 W/m^2 on DoY 93, 95, 96, and 97. This corresponds to days when the model estimates of VSM at 2 cm were higher than observed, with RMSD of $0.0374 \text{ m}^3/\text{m}^3$ and bias of $0.036 \text{ m}^3/\text{m}^3$ (Figure 9). This overestimation in VSM, possibly due to improper initial conditions and/or improper precipitation inputs (see sections 6.1 and 7.2.2.5), would lead to lower estimates of soil albedo using equation (A6). The overestimation also results in higher LE estimates (Figures 5c and 5d) due to underestimated soil surface resistance using equation (D9). In both the coupled and the standalone models, LE is overestimated with RMSDs of $\sim 65 \text{ W/m}^2$ and biases of $\sim 15 \text{ W/m}^2$. These RMSDs are higher than the sensor uncertainty of $11\text{--}28 \text{ W/m}^2$ (Table 1) but are comparable with those expected from Figure 3 using the Pareto front from the early season (see section 7.1.2).

[40] Both the coupled and stand-alone models estimate similar sensible heat fluxes, with RMSDs of $\sim 47 \text{ W/m}^2$ and biases of $\sim 29 \text{ W/m}^2$ (Figures 5e and 5f). These RMSDs are lower than those obtained for LE. For the days when LE is positively biased (e.g., DoY 97, 98, 101, 102, and 103), the sensible heat flux is biased negatively, and vice versa. The overall RMSD for sensible heat fluxes could be due to slightly lower aerodynamic resistance and/or due to overestimation of soil temperature in both the models (Figure 10). The RMSDs between the models and observations for soil

temperature are <2.22 K. This positive bias (<1.7 K) in soil temperature in the beginning of the simulation could be due to improper initial conditions (see section 6.1).

[41] The estimated soil heat flux (Figures 5g and 5h) is overestimated during the day and underestimated at night. Because the magnitude of the latent and sensible heat flux biases exceeds that of the net radiation overestimation, the net effect is slightly underestimated soil heat flux is at 2 cm, with RMSDs of $\sim 48 \text{ W/m}^2$ and biases of $\sim -3 \text{ W/m}^2$.

7.2.2.2. Midseason: Intermediate Vegetation Cover

[42] This period included the next 20 d of the growing season, when the vegetation is partially covering the terrain (DoY 105–125). The canopy height was 17–73 cm, LAI was 0.2–1.82, and fractional vegetation cover was 0.22–1.00. Overall, the model performance is better during this growth stage compared to the previous stage, as expected from the Pareto fronts (Figure 3 and section 7.1.2).

[43] As the vegetation cover increased during this period, the residuals in net radiation decrease significantly, indicating the decreasing influence of soil albedo on radiation balance. The daytime residuals decrease from $\sim 80 \text{ W/m}^2$ before DoY 115 to $<30 \text{ W/m}^2$ after DoY 115 (Figures 6a and 6b). Because of the improved net radiation estimates (RMSD $\sim 27 \text{ W/m}^2$), and the decreasing influence of soil surface resistance, RMSDs in LE are lower during this stage than during the bare soil stage (compare Figures 5c, 5d, 6c, and 6d) even though VSM remains overestimated by similar amounts. The RMSD of $\sim 59 \text{ W/m}^2$ correspond to those expected from the Pareto front in Figure 3. Sudden increase in modeled LE (Figures 6c and 6d) and corresponding decrease in sensible heat flux (Figures 6e and 6f) on DoY 109 and 119 are due to increased evaporation following rain or irrigation events.

[44] Similarly low RMSDs and biases are found in sensible heat flux, soil heat flux, and soil temperature. Sensible heat flux is overestimated, but matches more closely with observations during this stage than during the bare soil stage (Figures 6e and 6f), with RMSDs of $\sim 57 \text{ W/m}^2$ and biases of $\sim 35 \text{ W/m}^2$. Soil heat flux remains overestimated during the day and underestimated at night, similar to the previous stage (Figures 6g and 6h). Overall, the 2 cm soil heat flux is underestimated with RMSD of $\sim 39 \text{ W/m}^2$ and biases of $\sim -6 \text{ W/m}^2$ and. This is reflected in the soil temperature (Figure 10) as a lower overestimation (RMSD <1.67 K and bias <0.67 K) than in the previous stage for the stand-alone LSP, and an underestimation (RMSD <1.47 K and a negative bias $>-0.91 \text{ K}$) in the case of the LSP-DSSAT model.

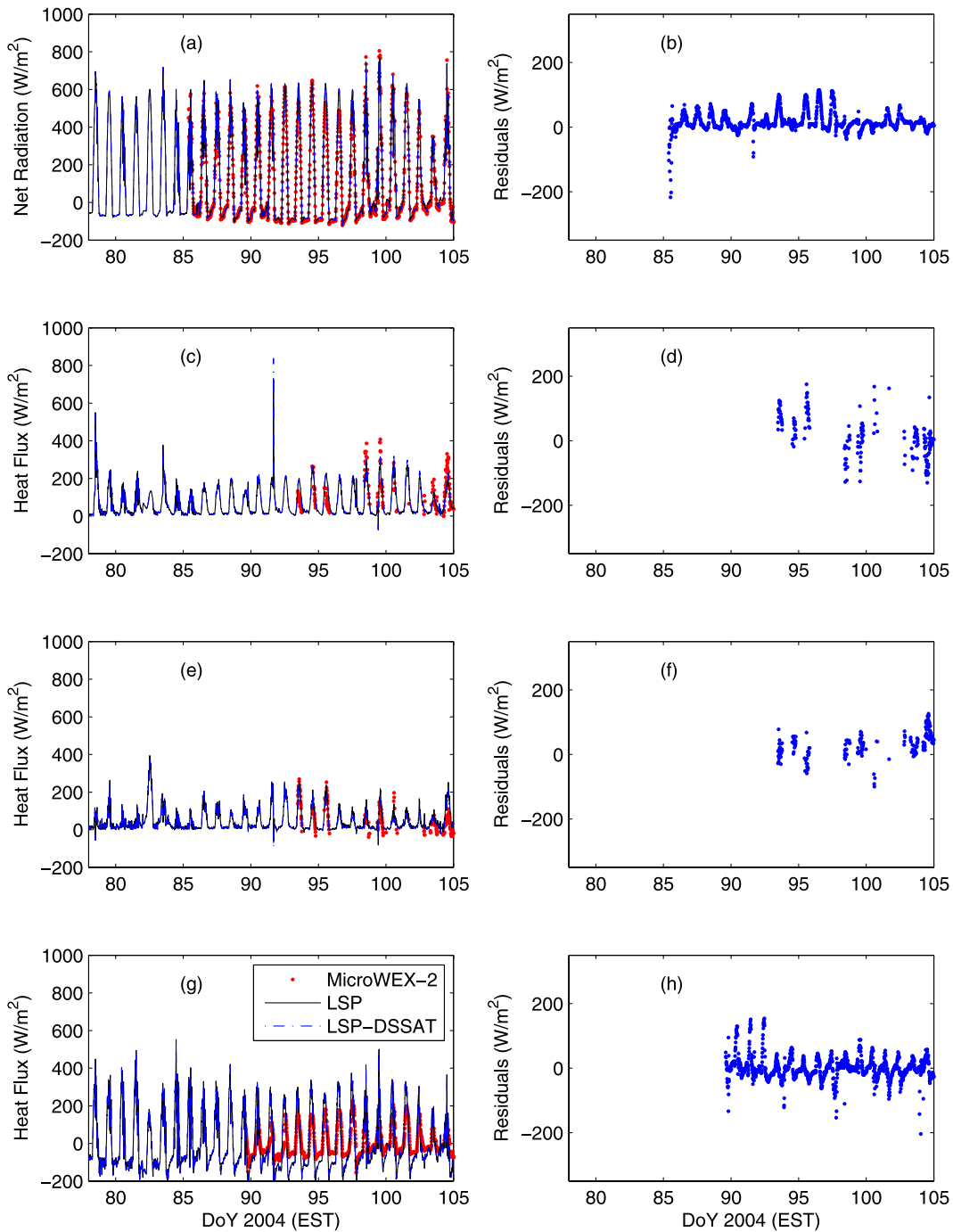


Figure 5. Comparison of fluxes estimated by the coupled LSP-DSSAT and stand-alone LSP model simulation and those observed during MicroWEX-2, between DoY 78 and 105: (a) net radiation, (b) net radiation residuals, (c) latent heat flux, (d) latent heat flux residuals, (e) sensible heat flux, (f) sensible heat flux residuals, (g) 2 cm soil heat flux, and (h) 2 cm soil heat flux residuals.

7.2.2.3. Late Season: Vegetative Stage

[45] This period included the next 10 d of the growing season, when the corn was in the vegetative growth stage and at full vegetation cover (DoY 125–135). The canopy height was 73–162 cm, LAI was 1.82–2.49, and vegetation cover was 1.00.

[46] In the previous stage, as vegetation cover increased, residuals for net radiation decreased. Because of full vegeta-

tion cover during this stage, net radiation (Figures 7a and 7b) matches very closely with observations, with RMSDs of ~ 16 W/m^2 and biases of ~ 8 W/m^2 , less than the estimated sensor uncertainty (Table 1). LE is overestimated with RMSD of ~ 62 W/m^2 and bias of ~ 3 W/m^2 (Figures 7c and 7d). The RMSD of ~ 62 W/m^2 correspond to the RMSD expected from the Pareto front in Figure 3. Though the net radiation matches well, it is still biased high, which would

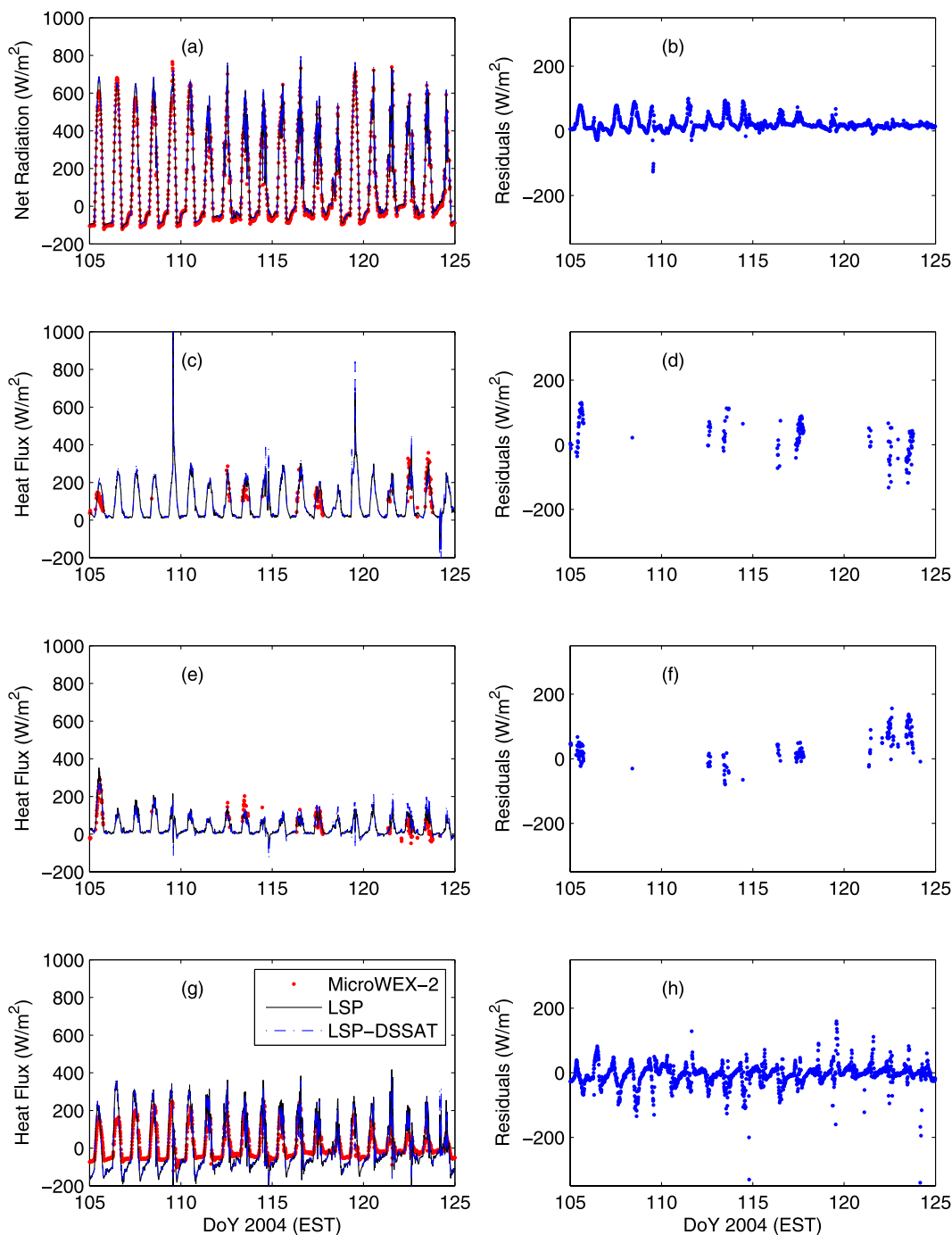


Figure 6. Comparison of fluxes estimated by the coupled LSP-DSSAT and stand-alone LSP model simulation and those observed during MicroWEX-2, between DoY 105 and 125: (a) net radiation, (b) net radiation residuals, (c) latent heat flux, (d) latent heat flux residuals, (e) sensible heat flux, (f) sensible heat flux residuals, (g) 2 cm soil heat flux, and (h) 2 cm soil heat flux residuals.

permit lower leaf surface vapor resistance by equations (D7) and (D8), resulting in overestimated LE from increased canopy transpiration. Overestimated VSM, shown in Figure 9, (RMSD $0.0492 \text{ m}^3/\text{m}^3$ and positive bias $0.0472 \text{ m}^3/\text{m}^3$) could also lead to overestimation of LE by increasing soil evaporation.

[47] Sensible heat flux (Figures 7e and 7f) is overestimated with RMSDs of $\sim 76 \text{ W/m}^2$ biases of $\sim 59 \text{ W/m}^2$.

This overestimation could be due to overestimated vegetation aerodynamic roughness length.

[48] The 2 cm soil heat flux (Figures 7g and 7h) is slightly overestimated with RMSD of $\sim 44 \text{ W/m}^2$ and bias of $\sim 0.70 \text{ W/m}^2$. Since during full cover, the net flux going into the soil is dominated by the flux between the soil and the canopy, the overestimation of soil heat flux indicates that soil-canopy flux is underestimated. This overestimation

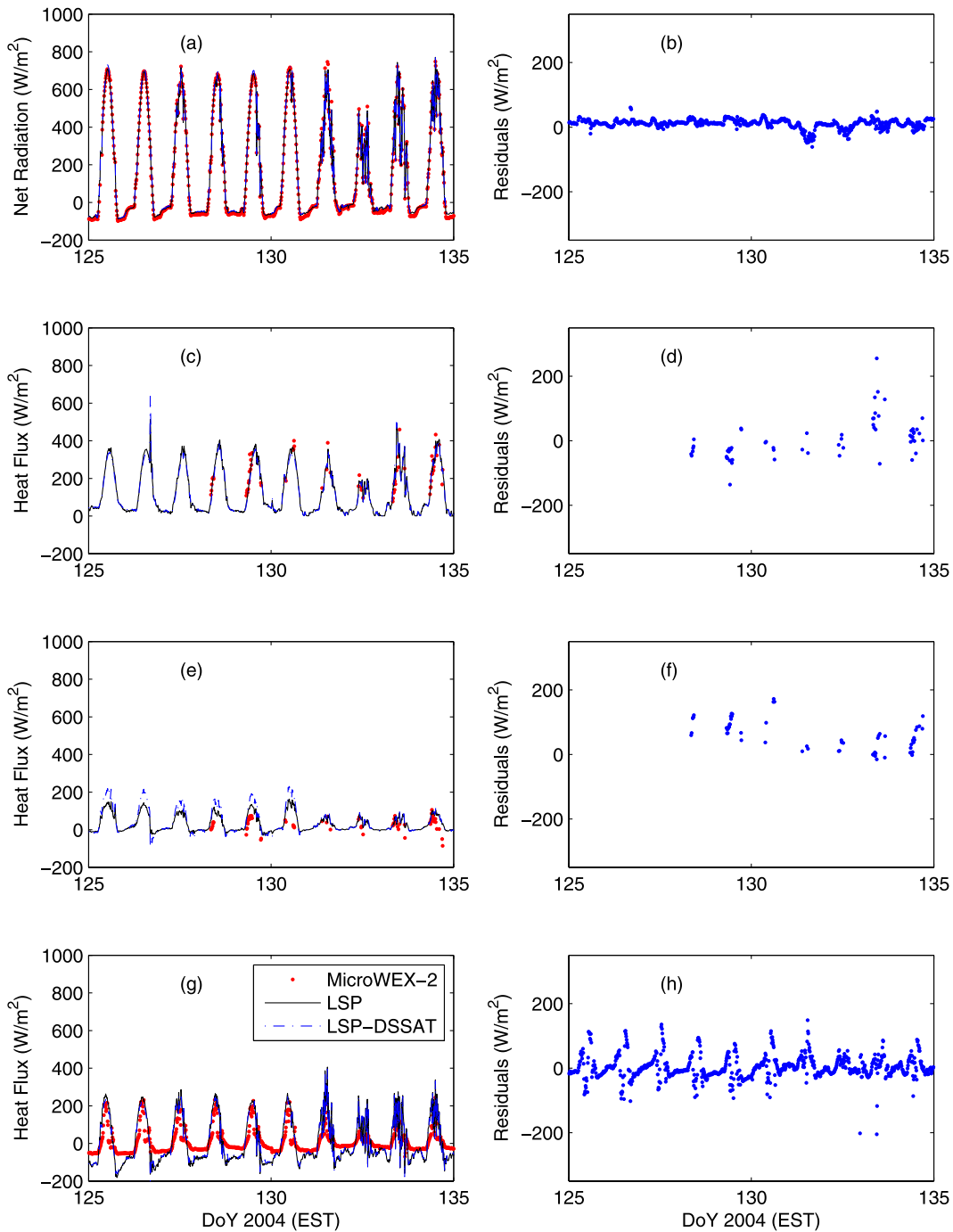


Figure 7. Comparison of fluxes estimated by the coupled LSP-DSSAT and stand-alone LSP model simulation and those observed during MicroWEX-2, between DoY 125 and 135: (a) net radiation, (b) net radiation residuals, (c) latent heat flux, (d) latent heat flux residuals, (e) sensible heat flux, (f) sensible heat flux residuals, (g) 2 cm soil heat flux, and (h) 2 cm soil heat flux residuals.

in soil heat flux leads to overestimation in soil temperature (Figure 10), more so than during intermediate vegetation cover, with a positive bias < 2.68 K and RMSD < 3.32 K.

7.2.2.4. Reproductive Stage

[49] The last 19 d of the growing season, DoY 135–154, comprised the reproductive stage, beginning with silk formation. During this period, the canopy height was 162–200 cm, LAI was 2.49–2.75, and vegetation cover was 1.00. The biomass growth during this stage was primarily due to ear growth.

[50] Similar to the previous stage, net radiation matches very closely with observations, with RMSDs of ~ 17 W/m^2 and biases of ~ 2.6 W/m^2 . The LE and H comparison could not be presented due to missing observations during this period.

[51] The 2 cm soil heat flux is slightly overestimated with RMSDs of ~ 55 W/m^2 and biases of ~ 2.3 W/m^2 , for similar reasons as during the nonreproductive full cover period. The overestimation in soil heat flux leads to overestimation in

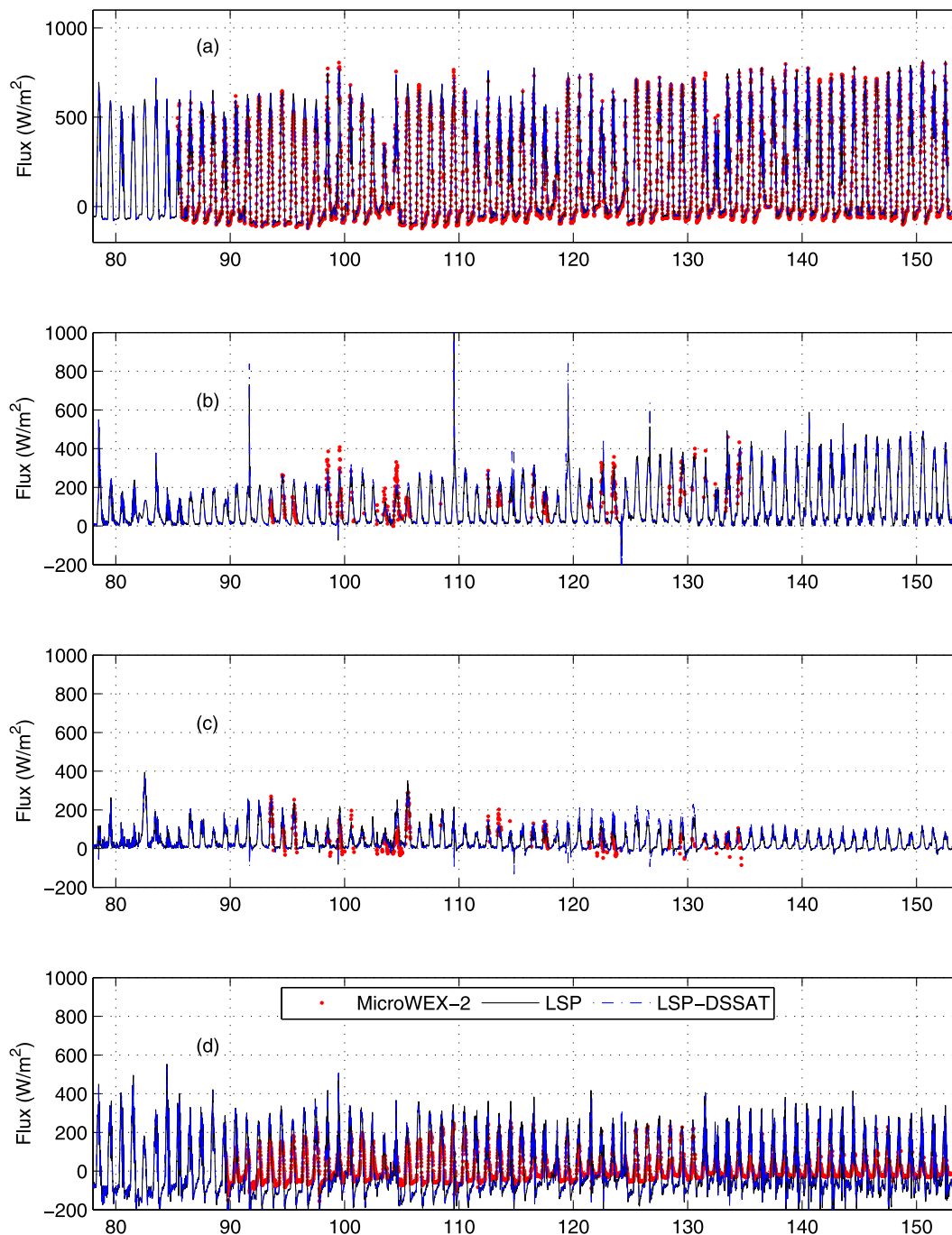


Figure 8. Comparison of fluxes estimated by the coupled LSP-DSSAT, by the stand-alone LSP model simulation, and those observed during MicroWEX-2: (a) net radiation, (b) latent heat flux, (c) sensible heat flux, and (d) 2 cm soil heat flux.

soil temperature (Figure 10), with RMSD < 3.39 K and a positive bias < 3.39 K.

[52] VSM (Figure 9) is overestimated with RMSD $0.0632 \text{ m}^3/\text{m}^3$ and a positive bias 0.0623 . The overestimation could be due to incorrect precipitation inputs, or accumulated moisture because of underestimated hydraulic conductivity in the bottom clay layer.

7.2.2.5. Growing Season: Planting to Harvest

[53] The coupled LSP-DSSAT model estimates radiation, fluxes, and soil moisture and temperature profiles that are very similar to those estimated by the stand-alone LSP

model with observed vegetation parameters for the growing season, as shown in Figures 8, 9, and 10 and Tables 9, 10, and 11. The RMSDs for the fluxes from the LSP-DSSAT model are slightly higher (by $\sim 3 \text{ W/m}^2$) than those from the LSP model, primarily because modeled canopy characteristics used in the LSP-DSSAT model rather than observations. For instance, LSP-DSSAT overestimates LAI by 0.29 , compared to the stand-alone DSSAT, which overestimates by 0.06 (Figure 4b), increasing canopy interception and net radiation.

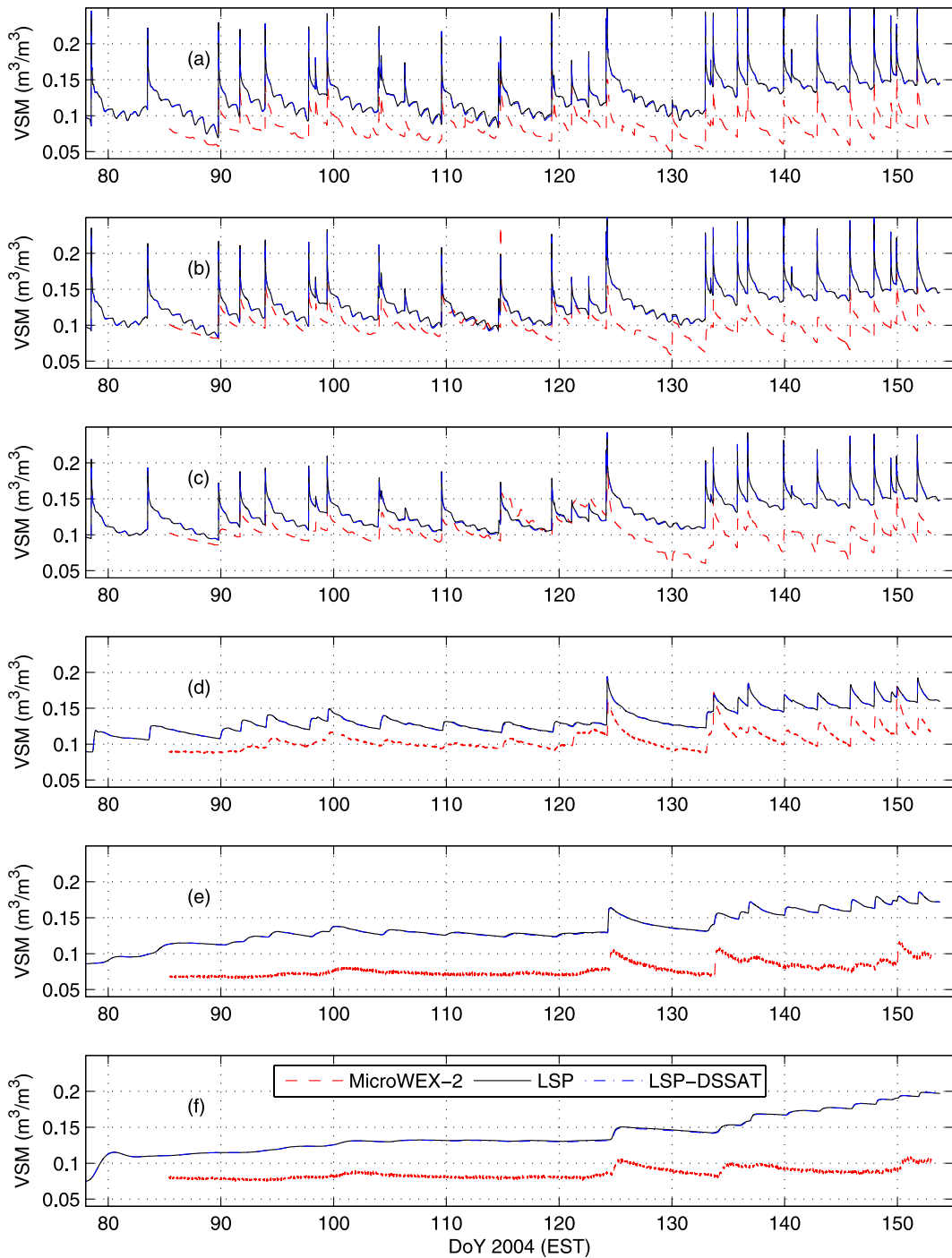


Figure 9. Comparison of volumetric soil moisture estimated by the coupled LSP-DSSAT, by the stand-alone LSP model simulation, and those observed during MicroWEX-2: (a) 2 cm, (b) 4 cm, (c) 8 cm, (d) 32 cm, (e) 64 cm, and (f) 100 cm.

[54] Overall, both the LSP and LSP-DSSAT models capture the diurnal variations and phases for net radiation (Figure 8a) throughout the growing season. The RMSDs between the LSP-DSSAT and observed net radiation are $\sim 24 \text{ W/m}^2$. These differences are close to the sensor uncertainty of 22 W/m^2 in Table 1. The biases are $\sim 17 \text{ W/m}^2$ indicate an overestimation. LE RMSDs of $\sim 62 \text{ W/m}^2$ are what can be expected from the Pareto front in Figure 3. Sudden increases in LE on DoY 93, 109, 119,

and 127, as shown in Figure 8b, are due to high evaporation after rainfall or irrigation. The RMSDs of $\sim 56 \text{ W/m}^2$ for sensible heat flux (Figure 8c) are lower than those for LE. The model overestimates the diurnal amplitude for soil heat flux at 2 cm (Figure 8d), with RMSDs of $\sim 47 \text{ W/m}^2$, due to daytime overestimation of net radiation.

[55] The RMSD for VSM at 2 cm (Figure 9 and Table 10) is similar to our choice of $0.043 \text{ m}^3/\text{m}^3$ on the overall season Pareto front (Figure 3). For both the LSP and LSP-DSSAT

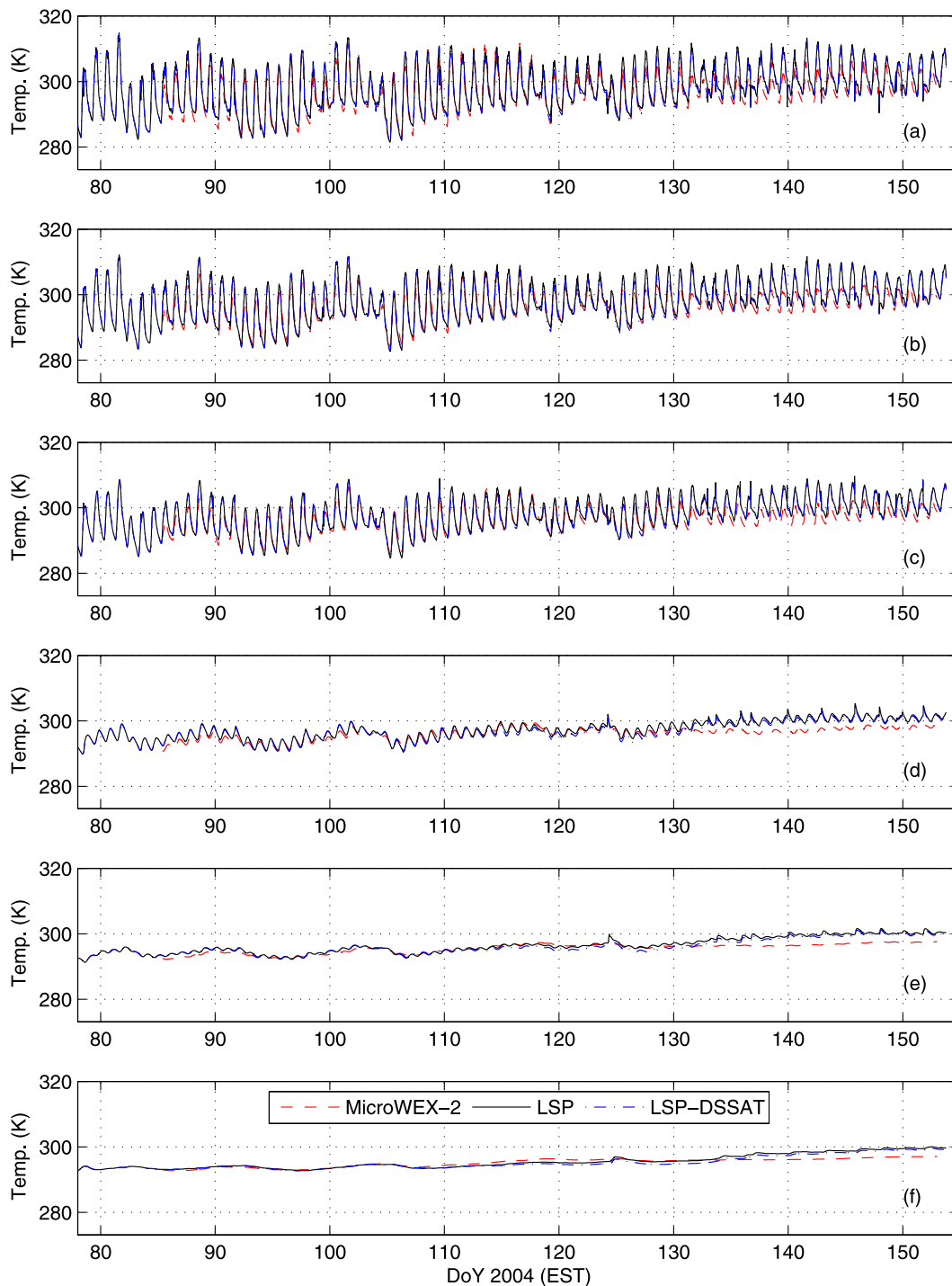


Figure 10. Comparison of soil temperature estimated by the coupled LSP-DSSAT, by the stand-alone LSP model simulation, and those observed during MicroWEX-2: (a) 2 cm, (b) 4 cm, (c) 8 cm, (d) 32 cm, (e) 64 cm, and (f) 100 cm.

model simulations, the VSMs at all layers exhibit positive bias that increases during the season. A bias of $\sim 0.02 \text{ m}^3/\text{m}^3$ could be introduced at the beginning of the simulation due to improper initial conditions (section 6.1) and significant uncertainty in rain gauge observations. During MicroWEX-2, we found that the differences between daily accumulations from the four rain gauge observations and those observed independently by using collection cans were

up to 10 s of mm/d. Previous studies have also found similarly high uncertainties in precipitation, at 12 mm/h, using such rain gauges [Nyustén *et al.*, 1996].

[56] The VSM bias of $\sim 0.06 \text{ m}^3/\text{m}^3$ for the layers 0.64 m and below (Figures 9e and 9f) could be due to the improper retention curve parameters in the clay layer (below 1.7 m). The parameters were based only on one soil sample from that layer and could have resulted in lower flux estimates at

the lower boundary and higher biases for the deeper layers. The decrease in drainage could also cause positive bias in VSM for the upper layers, closer to the land surface.

[57] Overall, soil temperatures (Figure 10) for both model simulations match closely with the MicroWEX-2 observations. During the bare soil period, soil temperature exhibits positive bias of <1.40 K and this bias is reduced during the intermediate vegetation cover period to <0.91 K due to a net reduction of soil heat flux estimates. As the soil heat flux bias increases, the temperature bias increases to <2.7 K after DoY 125. The seasonal RMSDs decrease with depth with a maximum of 2.43 K (Table 11).

8. Conclusion

[58] We calibrate a coupled SVAT-crop model to simulate energy and moisture fluxes at the land surface and in the vadose zone using a detailed, high temporal frequency data set for a growing season of sweet corn. The LSP model is calibrated with Latin Hypercube Sampling to provide the least root mean square difference (RMSD) between modeled and observed LE with an RMSD in VSM at 2 cm of $\sim 0.043 \text{ m}^3/\text{m}^3$. Model estimates of surface fluxes, VSM, and soil temperature were very similar using both the coupled LSP-DSSAT and stand-alone LSP that used observed vegetation parameters. This indicates that the moisture and energy fluxes can be modeled realistically for growing vegetation using coupled SVAT-crop models that do not require in situ observations of vegetation parameters. Because the model coupling was achieved without changing either of the models structurally, the techniques presented in this study can be extended to coupling of other SVAT and vegetation growth models.

Appendix A: Solar Radiation ($R_{s,c}$ and $R_{s,s}$)

[59] Downwelling solar radiation is partitioned between the soil ($R_{s,s}$) and canopy ($R_{s,c}$) by first dividing total solar radiation into direct and diffuse components, as an empirical function of clearness index and apparent solar time [Boland *et al.*, 2001]. The direct fraction is either transmitted, reflected, or absorbed. The net solar radiation absorbed by the canopy and soil are

$$R_{s,c} = \left[(1 - f_d)(1 - \tau_{c,dir})(1 - \rho_{c,dir}) + (f_d)(1 - \tau_{c,diff})(1 - \rho_{c,diff}) \right] R_{s,down} \quad (\text{A1})$$

$$R_{s,s} = (1 - \rho_s) \left[(1 - f_d)(\tau_{c,dir})(1 - \rho_{c,dir}) + (f_d)(\tau_{c,diff})(1 - \rho_{c,diff}) \right] R_{s,down} \quad (\text{A2})$$

where f_d is the diffuse fraction, $\tau_{c,dir}$ is the direct canopy transmissivity, $\tau_{c,diff}$ is the diffuse canopy transmissivity, $\rho_{c,dir}$ is the direct canopy reflectance, $\rho_{c,diff}$ is the diffuse canopy reflectance, ρ_s is the soil reflectance, and $R_{s,down}$ is the downwelling solar radiation.

[60] The direct canopy transmissivity is $\tau_{c,dir}$, given by Campbell and Norman [1998]:

$$\tau_{c,dir} = e^{-K(x,\Theta)\sqrt{1-\sigma}\Omega LAI} \quad (\text{A3})$$

where $K(x, \Theta)$ is the canopy extinction coefficient for canopy with an ellipsoidal leaf angle distribution, σ is the reflectance of a single leaf, x is the leaf angle distribution parameter, Θ is the solar zenith angle, LAI is the leaf area index of the canopy, and Ω is the clumping factor which accounts for incomplete canopy cover.

[61] The canopy reflectance is calculated as

$$\rho_{c,dir} = \frac{2K(x, \Theta)}{1 + K(x, \Theta)} \frac{1 - \sqrt{1 - \sigma}}{1 + \sqrt{1 - \sigma}} \quad (\text{A4})$$

The diffuse canopy transmissivity, $\tau_{c,diff}$, is found by integrating $\tau_{c,dir}$ over all solar zenith angles. Diffuse canopy reflectance $\rho_{c,diff}$ is given by Goudriaan [1977]:

$$\rho_{c,diff} = \frac{1 - \sqrt{1 - \sigma}}{1 + \sqrt{1 - \sigma}} \quad (\text{A5})$$

Radiation transmitted by the canopy is either reflected or absorbed by the soil according to the soil albedo, ρ_s . Soil albedo is a function of solar zenith angle and soil moisture [Idso *et al.*, 1975]. In this study, ρ_s is an empirical function of soil moisture, derived from MicroWEX-2 bare-soil data:

$$\rho_s = 0.0854e^{[-\max(\theta_s - 0.0532, 0)^2/0.0037]} + 0.14650 \quad (\text{A6})$$

where θ_s is the surface volumetric soil moisture (m^3/m^3).

Appendix B: Longwave Radiation ($R_{l,c}$ and $R_{l,s}$)

[62] The net longwave radiation absorbed by the canopy ($R_{l,c}$) and soil ($R_{l,s}$) are given by Kustas and Norman [2000]:

$$R_{l,c} = (1 - \tau_l)R_{l,down} + (1 - \tau_l)\epsilon_s\sigma_{sb}T_s^4 - 2(1 - \tau_l)\epsilon_c\sigma_{sb}T_c^4 \quad (\text{B1})$$

$$R_{l,s} = (\tau_l)R_{l,down} - \epsilon_s\sigma_{sb}T_s^4 + (1 - \tau_l)\epsilon_c\sigma_{sb}T_c^4 \quad (\text{B2})$$

where σ_{sb} is the Stefan-Boltzmann constant, $R_{l,down}$ is the downwelling longwave radiation, ϵ_s is the soil emissivity, ϵ_c is the canopy emissivity, and T_s and T_c are the soil and canopy temperatures in Kelvin. τ_l is the longwave canopy transmissivity, the integral over the hemisphere of direct transmissivity with σ as zero.

Appendix C: Sensible Heat Fluxes

[63] Figure C1 shows the resistance network model used to estimate sensible heat flux (H) at the surface. The sensible heat fluxes between the soil and air (H_{sa}), soil and canopy (H_{sc}), and canopy and air (H_{ca}), are calculated as:

$$H_{sa} = \rho_a c p_a \frac{T_s - T_a}{r_{as}} f_B \quad (\text{C1})$$

$$H_{sc} = \rho_a c p_a \frac{T_s - T_c}{r_{sc} + r_{bh}} f_V \quad (\text{C2})$$

$$H_{ca} = \rho_a c p_a \frac{T_s - T_c}{r_{ac} + r_{bh}} f_V \quad (\text{C3})$$

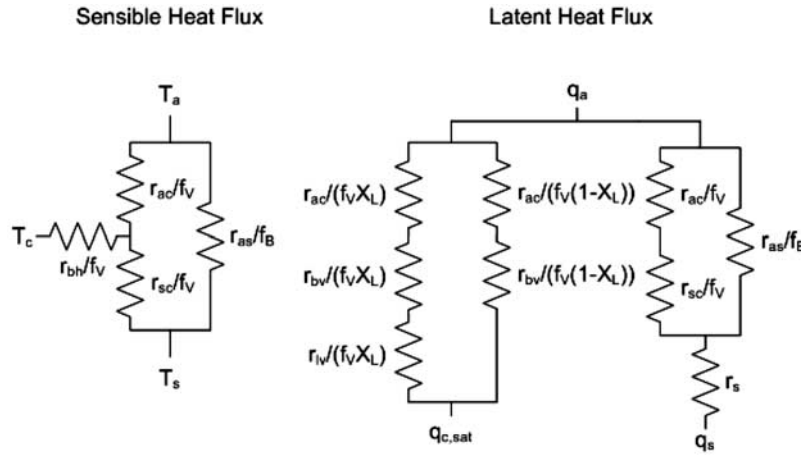


Figure C1. Surface resistance network to estimate sensible and latent heat fluxes in the LSP model.

where T_a , T_s , and T_c are the air, soil, and canopy temperatures (K), respectively, ρ_a is the air density (kg/m^3), cp_a is the specific heat (J/kg K), f_v and f_B are the vegetation and bare soil cover fractions, respectively.

[64] The aerodynamic resistances r_{as} (soil-air) and r_{ac} (canopy-air) are determined assuming a log wind profile above the canopy or bare soil [Goudriaan, 1977]:

$$r_{as} = \frac{\ln\left(\frac{z}{z_{ob}}\right) + \Psi_H}{ku^*} \quad (\text{C4})$$

$$r_{ac} = \frac{\ln\left(\frac{z-d}{z_{ov}}\right) + \Psi_H}{ku^*} \quad (\text{C5})$$

$$u^* = \frac{ku(z)}{\ln\left(\frac{z-d}{z_{ov}}\right) + \Psi_M} \quad (\text{C6})$$

where u^* is the friction velocity, Ψ is the Businger-Dyer stability function [Dyer, 1974], k is von Karman's constant (0.4), z is the measurement height, d is the vegetation displacement height (taken as $0.63h_c$, h_c is the plant canopy height), z_{ov} is the vegetation roughness length ($0.1h_c$), and z_{ob} is the bare soil roughness length.

[65] For the aerodynamic resistance between the soil and the canopy, the log profile is not valid due to momentum absorption by the canopy elements, so an exponential wind profile in the canopy is used [Goudriaan, 1977], with the under-canopy resistance, r_{sc} , from Niu and Yang [2004]:

$$r_{sc} = \frac{h_c}{aK_h} \left[e^{a(1-z_{ob}/h_c)} - e^{a(1-z_{ov}/h_c)} \right] \quad (\text{C7})$$

where a and K_h are the canopy damping coefficient and the aerodynamic conductance for heat at the top of the canopy [Goudriaan, 1977], given by:

$$a = \sqrt{\frac{c_d LAI h_c}{2l_m i_w}} \quad (\text{C8})$$

where

$$l_m = 2\sqrt[3]{\frac{0.75w_c^2 h_c}{\pi LAI}} \quad (\text{C9})$$

$$K_h = ku^* (h_c - d) \quad (\text{C10})$$

where, l_m is the canopy momentum length, i_w is the wind intensity factor, c_d is the drag coefficient, and w_c is canopy width. The leaf boundary layer resistances for heat transport, r_{bh} , is calculated as:

$$r_{bh} = \frac{1}{2} (180) \sqrt{\frac{l_w}{u_c}} \quad (\text{C11})$$

$$u_c = ku^* \ln\left(\frac{h_c - d}{z_{ov}}\right) \quad (\text{C12})$$

Appendix D: Latent Heat Flux

[66] Latent heat flux is based upon the resistance network (see Figure C1). Three sources that contribute to the flux are: soil evaporation (LE_s), canopy transpiration (LE_{tr}), and evaporation of intercepted precipitation (LE_{ev}).

$$LE_s = \lambda \rho_a (q_s - q_a) \left(\frac{f_v}{r_s + r_{sc} + r_{ca}} + \frac{f_B}{r_s + r_{as}} \right) \quad (\text{D1})$$

$$LE_{tr} = \lambda \rho_a (q_{c,sat} - q_a) \left[\frac{f_v(1-x_l)}{r_{ac} + r_{bv} + r_{tw}} \right] \quad (\text{D2})$$

$$LE_{ev} = \lambda \rho_a (q_{c,sat} - q_a) \frac{f_v x_l}{r_{ac} + r_{bv}} \quad (\text{D3})$$

where q_a , q_s , and $q_{c,sat}$ are the specific humidities of the air, soil surface layer, and saturated canopy, respectively, λ is the latent heat of vaporization of water, and x_l is the fraction

of vegetation covered in intercepted precipitation, calculated by

$$x_l = \frac{W_r}{W_{r,\max}} \quad (\text{D4})$$

$$W_{r,\max} = 0.2LAI \quad (\text{D5})$$

where $W_{r,\max}$ is the maximum possible interception, and W_r is the intercepted moisture by the canopy [Verseghy et al., 1993]. r_{bv} is the leaf boundary layer moisture resistance. r_{lv} and r_s are surface vapor transport resistances for the leaves and soil, respectively, where l_w is leaf width. The leaf resistance is based on canopy assimilation [Goudriaan, 1977]:

$$r_{bv} = 0.93r_{bh} \quad (\text{D6})$$

$$r_{lv} = \frac{\Delta C_{CO_2}}{1.66F_n} - .783r_{bh} \quad (\text{D7})$$

$$F_n = \left(1 - e^{R_{s,c\epsilon_{photo}}/F_m}\right)(F_m - F_d) + F_d \quad (\text{D8})$$

where ΔC_{CO_2} is the concentration difference of CO_2 between the leaf and air, in kg/m^3 , ϵ_{photo} is the photosynthetic efficiency, F_n is the net assimilation ($kg\ CO_2/m^2s$), F_d is the base assimilation rate, determined by a Q_{10} relationship from parameter F_b , and F_m , the maximum assimilation rate, is estimated as $10F_d$.

[67] Soil surface resistance is a linear function of surface moisture deficit [Camillo and Gurney, 1986],

$$r_s = soil_a\Delta\theta + soil_b \quad (\text{D9})$$

where moisture deficit ($\Delta\theta$) is the difference between saturated moisture content and actual moisture content.

[68] **Acknowledgments.** This research was supported by the NSF Earth Science Directorate (EAR-0337277) and the NASA New Investigator Program (NASA-NIP-00050655). The authors would like to thank the anonymous reviewers and Gabriel Katul for providing constructive suggestions to improve the manuscript. They also thank Orlando Lanni and Larry Miller for providing engineering support during MicroWEX-2; Jim Boyer and his team at PSREU for land and crop management; and Kai-Jen Tien, Tzu-Yun Lin, and Mi-Young Jang for their help in data collection during MicroWEX-2. The authors acknowledge computational resources and support provided by the University of Florida High-Performance Computing Center for the model calibration in this study.

References

- Boland, J., L. Scott, and M. Luther (2001), Modelling the diffuse fraction of global solar radiation on a horizontal surface, *Environmetrics*, 12, 103–116.
- Camillo, P., and R. J. Gurney (1986), A resistance parameter for bare soil evaporation models, *Soil Sci.*, 141, 95–105.
- Campbell Scientific (2006), CS616 and CS625 water content reflectometers, *Tech. Rep.*, Logan, Utah. (Available at <http://www.campbellsci.com/documents/manuals/cs616.pdf>)
- Campbell, G. S., and J. M. Norman (1998), *An Introduction to Environmental Biophysics*, 2nd ed., 286 pp., Springer, New York.
- Casanova, J. J., J. Judge, and J. W. Jones (2006), Calibration of the CERES-Maize model for linkage with a microwave remote sensing model, *Trans. ASAE*, 49(3), 783–792.
- Chung, Y. (2007), A snow-soil-vegetation-atmosphere-transfer/radiobrightness model for wet snow, Ph.D. thesis, Univ. of Michigan, Ann Arbor, Michigan.
- Dai, Y., et al. (2003), The Common Land Model (CLM), *Bull. Am. Meteorol. Soc.*, 84(8), 1013–1023.
- de Vries, D. A. (1963), Thermal properties of soils, in *Physics of Plant Environment*, edited by W. R. van Wijk, chap. 7, pp. 210–235, Elsevier, New York.
- Dyer, A. J. N. (1974), A review of flux-profile relationships, *Boundary Layer Meteorol.*, 7(3), 363–372.
- Entekhabi, D., et al. (2004), The hydrosphere (HYDROS) satellite mission: An earth system pathfinder for global mapping of soil moisture and land freeze thaw, *IEEE Trans. Geosci. Remote Sens.*, 42(10), 2184–2195.
- Garcia-Quijano, J. F., and A. P. Barros (2005), Incorporating physiology into a hydrological model: Photosynthesis, dynamic respiration, and stomatal sensitivity, *Ecol. Modell.*, 185, 29–49.
- Goudriaan, J. (1977), *Crop Micrometeorology: A Simulation Study*, 1st ed., 249 pp., Centre for Agricultural Publishing and Documentation, Wageningen, Netherlands.
- Gupta, H. V., L. A. Bastidas, S. Sorooshian, W. J. Shuttleworth, and Z. L. Yang (1999), Parameter estimation of a land surface scheme using multi-criteria methods, *J. Geophys. Res.*, 104(D16), 19,491–19,503.
- Idso, S., R. Jackson, R. Reginato, B. Kimball, and F. Nakayama (1975), The dependence of bare soil albedo on soil water content, *J. Appl. Meteorol.*, 14(1), 109–113.
- Jones, C., and J. Kiriya (Eds.) (1986), *CERES-Maize: A Simulation Model of Maize Growth and Development*, Texas A&M Univ. Press, College Station, Texas.
- Jones, J. W., G. Hoogenboom, C. Porter, K. Boote, W. B. L. Hunt, P. Wilkens, U. Singh, A. Gijsman, and J. Ritchie (2003), The DSSAT cropping system model, *Eur. J. Agron.*, 18(3–4), 235–265.
- Judge, J., A. England, C. L. W. Crosson, B. Hornbuckle, D. Boprie, E. Kim, and Y. Liou (1999), A growing season land surface process/radiobrightness model for wheat-stubble in the southern great plains, *IEEE Trans. Geosci. Remote Sens.*, 37(5), 2152–2158.
- Judge, J., L. Abriola, and A. England (2003), Development and numerical validation of a summertime land surface process and radiobrightness model, *Adv. Water Resour.*, 26(7), 733–746.
- Judge, J., J. J. Casanova, T. Lin, K. C. Tien, M. Jang, O. Lanni, and L. W. Miller (2005), Field observations during the second microwave, water, and energy balance experiment (MicroWEX-2): from March 17 through June 3, 2004. Circular no. 1480, *Tech. Rep.*, Center for Remote Sensing, University of Florida, Gainesville, Florida, USA. (Available at <http://edis.ifas.ufl.edu/AE360>)
- Judge, J., A. W. England, J. R. Metcalfe, D. McNichol, and B. E. Goodison (2008), Calibration of an integrated land surface process and radiobrightness (LSP/R) model during summertime, *Adv. Wat. Resour.*, 31(1), 189–202.
- Kerr, Y. H., P. Waldteufel, J. Wigneron, J. Martinuzzi, J. Font, and M. Berger (2001), Soil moisture retrieval from space: The Soil Moisture and Ocean Salinity (SMOS) mission, *IEEE Trans. Geosci. Remote Sens.*, 39(8), 1729–1735.
- Kustas, W. P., and J. M. Norman (2000), A two-source energy balance approach using directional radiometric temperature observations for sparse canopy covered surfaces, *Agron. J.*, 92, 847–854.
- Leese, J., T. Jackson, A. Pitman, and P. Dirmeyer (2001), GEWEX/BAHC international workshop on soil moisture monitoring, analysis, and prediction for hydrometeorological and hydroclimatological applications, *Bull. Am. Meteorol. Soc.*, 82(7), 1423–1430.
- Liou, Y., J. Galantowicz, and A. England (1998), A land surface process/radiobrightness model with coupled heat and moisture transport for freezing soils, *IEEE Trans. Geosci. Remote Sens.*, 36(2), 669–677.
- Lizaso, J. I., W. D. Batchelor, K. J. Boote, and M. E. Westgate (2005), Development of a leaf-level canopy assimilation model for CERES-Maize, *Agron. J.*, 97, 722–733.
- McKay, M. D., R. J. Beckman, and W. J. Conover (2000), A comparison of three methods for selecting values of input variables in the analysis of output from a computer code, *Technometrics*, 42(1), 55–61.
- Mo, X., S. Liu, Z. Lin, Y. Xu, Y. Xiang, and T. McVicar (2005), Prediction of crop yield, water consumption and water use efficiency with a SVAT-crop growth model using remotely sensed data from the north china plain, *Ecol. Modell.*, 183, 301–322.
- Niu, G.-Y., and Z.-L. Yang (2004), Effects of vegetation canopy processes on snow surface energy and mass balances, *J. Geophys. Res.*, 109, D23111, doi:10.1029/2004JD004884.
- Nyusten, J. A., J. R. Front, P. G. Black, and J. C. Wilkerson (1996), A comparison of automatic rain gauges, *J. Atmos. Oceanic Technol.*, 13(1), 62–73.

- Omega (2006), Thermistor elements and compatible instrumentation, *Tech. Rep.* (Available at http://www.omega.com/Temperature/pdf/44000_THERMIS_ELEMENTS.pdf)
- Pan, H.-L., and L. Mahrt (1987), Interaction between soil hydrology and boundary layer development, *Boundary Layer Meteorol.*, *38*, 185–202.
- Philip, J. R., and D. A. de Vries (1957), Moisture movement in porous material under temperature gradients, *Trans. Am. Geophys. Union*, *38*, 222–232.
- Richardson, A., et al. (2006), A multi-site analysis of random error in tower-based measurements of carbon and energy fluxes, *Agric. For. Meteorol.*, *136*(1–2), 1–18.
- Rossi, C., and J. R. Nimmo (1994), Modeling of soil water retention from saturation to oven dryness, *Water Resour. Res.*, *30*, 701–708.
- Twine, T., W. P. Kustas, J. M. Norman, D. R. Cook, P. R. Houser, T. P. Meyers, J. H. Prueger, P. J. Starks, and M. L. Wesely (2000), Correcting eddy-covariance flux underestimates over a grassland, *Agric. For. Meteorol.*, *103*, 279–300.
- Verseghy, D. L., N. A. McFarlane, and M. Lazare (1993), Class - a Canadian land surface scheme for GCMs II. Vegetation model and coupled runs, *Int. J. Climatol.*, *13*, 347–370.
- Whitfield, B., J. Jacobs, and J. Judge (2006), Intercomparison study of the land surface process model and the common land model for a prairie wetland in Florida, *J. Hydrometeorol.*, *7*(6), 1247–1258.

J. J. Casanova and J. Judge, Center for Remote Sensing, Agricultural and Biological Engineering Department, Institute of Food and Agricultural Sciences, University of Florida, 275 Rogers Hall, 1 Museum Road, Gainesville, FL 32611, USA. (jasmeet@ufl.edu)